# Accepted Manuscript

CuMnO$_2$-reduced graphene oxide nanocomposite as a free-standing electrode for high-performance supercapacitors

Farzaneh Bahmani, Sayeh Habib Kazemi, Yuhan Wu, Long Liu, Yang Xu, Yong Lei

Please cite this article as: F. Bahmani, S.H. Kazemi, Y. Wu, L. Liu, Y. Xu, Y. Lei, CuMnO$_2$-reduced graphene oxide nanocomposite as a free-standing electrode for high-performance supercapacitors, *Chemical Engineering Journal* (2019), doi: https://doi.org/10.1016/j.cej.2019.121966

# CuMnO₂-reduced graphene oxide nanocomposite as a free-standing electrode for high-performance supercapacitors

Farzaneh Bahmani[a,b], Sayeh Habib Kazemi[a,*], Yuhan Wu[b], Long Liu[b], Yang Xu[b,*], and Yong Lei[b,*]

[a] Department of Chemistry, Institute for Advanced Studies in Basic Sciences (IASBS), Zanjan 45137-66731, Iran

[b] Fachgebiet Angewandte Nanophysik, Institut für Physik & ZMN MacroNano (ZIK), Technische Universität Ilmenau, Ilmenau 98693, Germany

* Corresponding authors:

E-mail: habibkazemi@iasbs.ac.ir. Tel: +98 2433153126.  (Sayed Habib Kazemi)

E-mail: yang.xu@tu-ilmenau.de. Tel: +49 03677694902. (Yang Xu)

E-mail: yong.lei@tu-ilmenau.de. Tel: +49 03677693748.  (Yong Lei)

**Abstract**

Free-standing electrodes have attracted wide attention for advanced supercapacitors. Herein, direct deposition of $CuMnO_2$ and $CuMnO_2$-reduced graphene oxide (rGO) nanocomposite on nickel foam (NF) substrates was performed through a simple hydrothermal process. The simultaneous deposition makes full use of the synergistic effect formed by the large pseudocapacitance of $CuMnO_2$ and excellent electrical conductivity of rGO, which results a greater performance improvement of the nanocomposite comparing with that of bare $CuMnO_2$. Remarkably, the $CuMnO_2$-rGO/NF electrode displays a large specific capacitance of 1727 F $g^{-1}$ at 3 A $g^{-1}$ and manifests exceptional cycling stability with a retention ratio of 125% of the initial capacitance over consecutive 5000 cycles. Furthermore, a rGO/NF//$CuMnO_2$-rGO/NF asymmetric supercapacitor exhibits great electrochemical performance by delivering high energy density (37.5 Wh $kg^{-1}$) and high power density (4250 W $kg^{-1}$) as well as excellent cycling stability (3.3% decay after 4000 cycles). The presented results suggest that $CuMnO_2$-rGO nanocomposite can be considered as a potential candidate for highly stable and high-rate supercapacitors.

## 1. Introduction

Designing clean and sustainable energy storage devices is one of the key challenges to humankind in the industrial age. Supercapacitors are emerging as an ideal candidate because of their potentially high-impact characteristics including high power density, long cycle life, rapid recharging capability and high reliability. However, they cannot supply a high energy density for large-scale applications[1-5]. Therefore, exploring high-quality electrode materials with a high energy density for supercapacitors has become an ongoing challenge for researchers. In this regard, metal oxides are highly desirable for high-performance supercapacitors owing to their high capacitance [6-8]. However, it has been observed that the low stability and unsatisfactory electronic conductivity of metal oxides undermine their overall effectiveness to deliver high performance. Therefore, hybrid materials consisting of metal oxides and carbonaceous materials have been extensively developed to address these issues, which relies on the combination of the unique properties of each component, including high capacitance, large surface area, and good electrical conductivity. Among various carbonaceous materials, graphene nanosheets are an excellent backbone to hold metal oxides because of their extraordinary properties such as excellent electrical conductivity, high surface area, and outstanding structural stability [9-11]. Accordingly, graphene-metal oxide composites have exhibited great rate capability and high reversibility [12, 13]. Ghosh et al. reported a specific capacitance of 928.43 F $g^{-1}$ at 5 A $g^{-1}$ for reduced graphene oxide (rGO)/BiFeO$_3$[14]. A high specific capacitance of 1813 F $g^{-1}$ at 2 A $g^{-1}$ for Graphene-wrapped CuCo$_2$O$_4$ was reported by Moosavifard et al [15]. Zhao et al. obtained a high specific capacitance of 1316 F $g^{-1}$ at 5 A $g^{-1}$ for Ni,Co−OH/rGO [16].

Recently, binary metal oxides have been intensively explored for energy storage applications, because they can deliver higher capacitive performance comparing with monometallic oxides, owing to richer redox reactions and a wider potential window [17-19]. A typical class of materials,

3

spinel-type manganese oxides ($MMn_2O_4$, M=Zn, Co, and Ni) [20-22], are of interest as active materials in supercapacitors due to extraordinary properties of manganese such as high theoretical capacitance, well-defined electrochemical redox activity, desired electrochemical performance and synergetic effect of manganese with M ions [20-25]. However, there has been rarely reported that $MMnO_2$-type manganese oxides can be used for supercapacitors. Recently, Liu et al reported $CuMnO_2$ nanoparticles as a new electrode material for symmetric supercapacitor [26], but the non-conductive binders used for the electrode fabrication reduces active surface area, hinders the wettability of the active material's surface towards the electrolyte, and reduces the electrical conductivity of the electrode [6, 27, 28]. For a nanostructured electrode material of supercapacitors, direct growth of the nanostructure on the current collector without binders is imperative, because it could ensure direct transport pathways to optimize rate capability and charge transport in the electrode.

In this work, we report a $CuMnO_2$-rGO nanocomposite directly growing on a nickel foam (NF) substrate through a facile hydrothermal approach followed by a subsequent annealing treatment. To the best of our knowledge, this work is the first report of a free-standing electrode containing $CuMnO_2$ for the supercapacitor application and the comparison between $CuMnO_2$-rGO/NF and $CuMnO_2$/NF electrodes. Our results revealed the excellent electrochemical performance (1727 and 1400 F $g^{-1}$ at 3 and 10 A $g^{-1}$, respectively) and long cycle life (5000 cycles) of the $CuMnO_2$-rGO/NF electrode. To the best of our knowledge, these results are the highest among all the $ABO_2$-type mixed metal oxides as supercapacitor electrodes. Furthermore, we constructed an asymmetric supercapacitor using $CuMnO_2$-rGO/NF as positive electrode and rGO/NF as negative electrode. The asymmetric supercapacitor delivered a high energy density of 37.5 Wh $kg^{-1}$ and power density of 4250 W $kg^{-1}$ as well as a long-term stability up to 4000 cycles.

## 2. Experimental

### 2.1 Synthesis of $CuMnO_2$/NF and $CuMnO_2$-rGO/NF electrodes

Graphite oxide (GO) was prepared by a modified Hummers method [29]. The synthesis of $CuMnO_2$-rGO nanocomposite on NF substrate was performed via a hydrothermal progress by immersing the pre-cleaned NF in an aqueous solution of $Cu(NO_3)_2 \cdot 6H_2O$ (0.5mmol), $Mn(CH_3OO)_2 \cdot 4H_2O$ (0.5mmol), urea (300 mg) and GO suspension (5 mg mL$^{-1}$) and being heated at 180°C for 24 h. The obtained electrodes were washed with ethanol and deionized water and dried at 80°C for 12 h. Finally, the as-prepared electrodes were annealed at 300°C for 2 h in an $N_2$ atmosphere with a heating rate of 3°C min$^{-1}$. A typical mass loading is 1 mg cm$^{-2}$. For comparison, $CuMnO_2$/NF was prepared under identical conditions, except for the replacement of GO suspension with deionized water.

### 2.2 Characterizations

The morphology and structure of the samples were characterized by scanning electron microscopy system (SEM, Hitachi S4800) equipped with EDX analyser, transmission electron microscopy (TEM, Philips TecnaiTM), powder X-ray diffraction (XRD, SIEMENS/BRUKER D5000, CuKα λ = 1.54 Å), Fourier transform infrared (FTIR Bruker Vector-22), X-ray photoelectron spectroscopy (XPS, VG-Microtech Multilab 3000), and Raman-AFM system (NT-MDT). Surface area and pore size distribution of the samples were measured by $N_2$ adsorption-desorption based on the Brauner-Emmet-Teller (BET) and Barrett-Joyner-Halenda (BJH) theory (Belsorp-BELMAX). Thermal gravimetric analysis (TGA) was conducted on a NETZSCH STA 409 PC/PG instrument with a rate of 10°C min$^{-1}$.

5

*2.3 Electrochemical measurements*

Electrochemical performances of the electrode materials were evaluated in both three- and two-electrode configuration with a 2 M of KOH electrolyte solution using an Autolab101 potentiostat (Eco. Chemie, the Netherlands) and a Zahner-Zennium potentiostat-galvanostat (Zahner, Germany) instruments. In addition, electrochemical impedance spectroscopy (EIS) measurement was carried out at the open-circuit potential in a frequency range from 100 kHz to 100 mHz. The complex nonlinear least square (CNLS) fitting method was implemented on the EIS experimental results to calculate the kinetic parameters. In a three-electrode system, $CuMnO_2$ or its nanocomposite was supported onto a piece of NF (1 cm$^2$), a Pt electrode and an Ag/AgCl electrode were used as working, counter and reference electrode, respectively. An asymmetric supercapacitor was assembled by using $CuMnO_2$-rGO/NF as positive electrode, rGO/NF as negative electrode and filter paper as separator. The specific capacitance (Cs) from cyclic voltammograms was calculated by the equation as below [30]:

$$C_s = \frac{\int I(V)dV}{m\Delta V S} \text{ (F g}^{-1}) \tag{1}$$

Where *I* is the response current, *S* is scan rate, *m* is mass of active material on the electrode, and *ΔV* is potential window in cyclic voltammetry. Power density (*P*) and energy density (*E*) are obtained from the galvanostatic discharge curves according to the following equations [31]:

$$C_s = \frac{I\Delta t}{m\Delta V} \text{ (F g}^{-1}) \tag{2}$$

$$E = \frac{0.5 C_s \Delta V^2}{3.6} \text{(Wh kg}^{-1}) \tag{3}$$

$$P = \frac{3600\, E}{\Delta t} \text{ (F g}^{-1}) \tag{4}$$

Where $I$ is the discharge current, $\Delta t$ is the full discharge time, and $\Delta V$ is the potential range of a full discharge.

## 3. Results and discussion

### 3.1 Morphological and structural analysis

CuMnO$_2$ and CuMnO$_2$-rGO nanocomposites were directly synthesized on the NF substrate without any binder or surfactant. The phase of the materials was ascertained from XRD analysis as presented in Fig. 1a. The observed diffraction peaks of both CuMnO$_2$ and CuMnO$_2$-rGO can be well indexed to CuMnO$_2$ (JCPDS 50-0860) without any impurity phases [26]. The absence of the rGO peak at $\sim 2\theta = 25°$ (Fig. S1) in the XRD pattern of the nanocomposite may be attributed to the weak diffraction intensity of rGO comparing to that of CuMnO$_2$. The coexistence of rGO and CuMnO$_2$ in the nanocomposite can be confirmed by the TG Analysis, Raman spectroscopy and X-ray photoelectron spectroscopy (will be discussed later). The composition of the CuMnO$_2$-rGO nanocomposite was studied by the TGA method as shown in Fig. 1b. CuMnO$_2$ displays only one weight loss below 350°C due to the removal of the physiosorbed water and structural water, while no weight loss was observed from 350-800°C, suggesting the thermal stability of CuMnO$_2$ under N$_2$ atmosphere [32]. The weight loss of rGO below 400°C could be ascribed to the loss of adsorbed water and the remaining carboxyl, hydroxyl, or epoxy groups. The destruction of the carbon skeleton of graphene leads to the relatively significant weight loss from 400 °C to 800°C [33, 34]. The mass ratio of rGO and CuMnO$_2$ in the nanocomposite is found to be 1:2.8 by the following formulas that is well matched with amount of using GO in experimental section:

$$m_{\text{CuMnO2}} \cdot \beta + m_{\text{rGO}} \cdot \gamma = m_{\text{CuMnO2 - rGO}} \cdot \alpha \qquad (5)$$

$$m_{\text{CuMnO2}} + m_{\text{rGO}} = m_{\text{CuMnO2 - rGO}} \qquad (6)$$

$$\frac{x}{y} = \frac{\alpha - \gamma}{\beta - \alpha} \qquad (7)$$

Where $x$ and $y$ is the mass ratio of $CuMnO_2$ and rGO in the nanocomposites, and $\beta$, $\alpha$ and $\gamma$ are residue percentages of $CuMnO_2$, $CuMnO_2$-rGO nanocomposite and rGO, respectively. In Fig. 1c, the Raman spectrum of $CuMnO_2$ displays a strong peak at 688 cm$^{-1}$ and two weak peaks at 332 and 386 cm$^{-1}$ that correspond to the stretching vibrations of the $CuMnO_2$ structure [26]. The two strong peaks at 1357 and 1600 cm$^{-1}$ of rGO are designed to D band and G band of carbon, respectively [35, 36]. The simultaneous appearance of carbon bands and $CuMnO_2$ peaks in the Raman spectrum of the nanocomposite demonstrates the coexistence of rGO and $CuMnO_2$. The relative intensity ratio of the D band to the G band (ID/IG) can be used to measure the reduction extent of GO. Notably, the value of ID/IG ratio for $CuMnO_2$-rGO nanocomposite (1.25) is higher than that of rGO (1.05), suggesting a more disordered structure due to the interfacial interactions of rGO with $CuMnO_2$ as well as an increasing in the number of smaller sp$^2$ domains [37-39]. The XPS survey spectrum of the nanocomposite (Fig. S2) confirms the existence of C, Mn, Cu and O. Fig. 1d shows the high-resolution XPS spectra of Cu 2p, Mn 2p and C 1s. In the Cu spectrum, two major peaks at 934.1 eV (Cu 2p3/2) and 953.8 eV (Cu 2p1/2) with a splitting energy of 19.7 eV prove the monovalent state of Cu ion [40, 41]. In the Mn spectrum, intense peaks at 641.7 eV (Mn 2p3/2) and 653.6 eV (Mn 2p1/2) with a splitting energy of 11.7 eV identify the $Mn^{3+}$ valance in the nanocomposite [26, 42]. The C1s spectrum can be resolved into four peaks at 284.6, 286.5, 287.4 and 288.9 eV, corresponding to C-C/C=C, C-OH, C=O and O-C=O, respectively [43].

Nitrogen adsorption-desorption isotherms of $CuMnO_2$ and $CuMnO_2$-rGO nanocomposite are shown in Fig. S3. Both materials depicted type IV isotherm with hysteresis loop, which is a property of the mesoporous materials [15]. The BET surface area studies confirm the increased surface area of nanocomposite (90.3 m$^2$ g$^{-1}$) compared with $CuMnO_2$ (54.9 m$^2$ g$^{-1}$) due to incorporation of rGO in the electrode material structure and the formation of secondary pores between the rGO nanosheets and $CuMnO_2$ nanoplates. The increased surface area can provide

higher number of active sites, desired electrical connection for fast rate of redox reaction and charge transfer, which could effectively improve energy storage ability. This observation is in good accord with the result of BJH pore size distribution (inset of Fig. S3), where the major size of the $CuMnO_2$-rGO nanocomposite is 4.6 nm that derives from the space between the $CuMnO_2$ nanoplates and rGO as well as the nanosheets themselves.

The morphology of the as prepared samples is depicted in Fig. 2. SEM images of the $CuMnO_2$/NF electrode reveal dense coverage of $CuMnO_2$ nanoplates with a thickness of 8-14 nm on the NF surface (Fig. 2a and 2b). The nanoplates directly grow on the NF surface without any block of polymer binders, which could lead to better ion insertion and electron transport at the electrode/electrolyte interface (Fig. S4). The directly formation of nanocomposite on the NF surface is displayed in Fig. S5. The SEM images of the $CuMnO_2$-rGO/NF electrode is show the presence of rGO nanosheets and $CuMnO_2$ nanoplates distributed on the surface of rGO (Fig. 2c, d). As shown in Fig. 2d, the flexibility of rGO can be seen from a few spots that are not covered by the nanoplates. The nanoplates display similar shape and thickness as shown in Fig. 2b, demonstrating that the incorporation of rGO does not affect the growth of $CuMnO_2$ nanoplates. The revealed combination of rGO nanosheets and $CuMnO_2$ nanoplates could enhance the surface area (Fig. S3) comparing with bare $CuMnO_2$ nanoplates and thus provide more electroactive sites for Faradaic reactions. Furthermore, the space between the nanoplates and rGO nanosheets can act as electrolyte transport channels during the charging/discharging process. Fig. S6 shows the SEM images of the $CuMnO_2$-rGO nanocomposite that partially peels off from the NF substrate, which clearly demonstrates the flexible rGO and its connection to the $CuMnO_2$ nanoplates. The coexistence of C, Cu, Mn and O elements in the nanocomposite is once again confirmed by the EDX spectra and EDX mapping analysis (Fig. S7). HRTEM method was utilized to further characterize the as-prepared $CuMnO_2$-rGO nanocomposite. Fig. 2e and 2f demonstrate the

9

nanoplate morphology of $CuMnO_2$, and once again the thinness of the nanosheets is proven by the low contrast in Fig. 2e. Side view of an individual nanosheet displays a thickness of 12 nm, which agrees with the results in Fig. 2b. A lattice fringe of 5.8 Å was observed (inset of Fig. 2f), which corresponds to the interlayer space of the (001) plane of $CuMnO_2$. To summarize the morphological and structural analysis, a $CuMnO_2$-rGO composite was successfully fabricated directly on a NF substrate. The composite is consisted of $CuMnO_2$ nanoplates and rGO nanosheets, where the former grows on the surface of the latter. The $CuMnO_2$-rGO/NF electrode is expected to deliver high performance as a free-standing electrode of supercapacitors owing to the synergetic effect formed by each component.

*3.2 Electrochemical analysis*

Cyclic voltammetry (CV) and galvanostatic charge/discharge (GCD) measurements were initially performed to elucidate the electrochemical performance of the as-prepared electrodes in a three-electrode system with a 2 M KOH electrolyte. Fig. 3a presents the comparison of CV curves of the $CuMnO_2$/NF and $CuMnO_2$-rGO/NF electrodes at a scan rate of 50 mV $s^{-1}$ within a voltage window of -0.2 to 0.7 V. Both electrodes display a pair of reversible redox peaks, suggesting a pseudo capacitive behavior that results from a reversible redox reaction between M-O/M-OH (M represents Cu and Mn) and OH$^-$ [26]. The remarkable augmentation in the integral CV area of the $CuMnO_2$-rGO/NF electrode comparing with the $CuMnO_2$/NF electrode is ascribed to the incorporation of the high surface area and conductivity of rGO, signifying the higher charge storage ability and substantial improvement of performance. It should be noted that the integrated area under the CV curves of bare Ni foam electrode is dramatically lower than that of the $CuMnO_2$/NF and $CuMnO_2$/rGO/NF electrodes; revealing the negligible contribution of capacitance of the NF substrate in total specific capacitance (Fig. S8). Also, after deposition of electrode materials on the

10

nickel foam surface, the area exposed to the electrolyte will be decreased and then the corresponding capacitance contribution from Ni foam will be lowered. The CV curves of the $CuMnO_2$/NF and $CuMnO_2$-rGO/NF electrodes at various scan rates are depicted in Fig. 3b and 3c. The specific capacitance values of the $CuMnO_2$-rGO/NF electrode were calculated to be 1574, 1527, 1450, 1351, 1261, 1183, 1131 and 1058 F $g^{-1}$ at 5, 10, 15, 20, 25, 30, 40 and 50 mV $s^{-1}$, respectively. The specific capacitance of the $CuMnO_2$/NF electrode was calculated to be 711, 685, 641, 610, 585, 539, 477 and 427 F $g^{-1}$ at the same scan rates. It is concluded that specific capacitance can be originated from the significant pseudocapacitance of $CuMnO_2$ that was enhanced by electric double layer capacitance (EDLC) of the rGO nanosheets. The specific capacitance decreases as the scan rate increases, which reflects the limited accessibility of ions into inner region at a short time scale [44]. The capacitance preservation at 50 mV $s^{-1}$ of the $CuMnO_2$/NF and $CuMnO_2$-rGO/NF electrodes were 60% and 67% of that at 5 mV $s^{-1}$, respectively. Besides, the positions of the redox peaks showed a slight shift upon increasing the scan rate owing to diffusion polarization effect [45], while these CV curves maintain a similar shape, indicating the considerable kinetic reversibility and rate capability of the composite.

Therefore, the obtained high capacitance for $CuMnO_2$-rGO nanocomposite referred to as pseudocapacitance and the non-Faradaic contribution from the double layer effect. These capacitive effects were characterized by analyzing the voltammetric data at various sweep rates according [46]:

$$i = av^{1/2} \quad \text{or} \quad Log\,(i) = Log(a) + b\,Log(v) \tag{8}$$

where a and b are adjustable parameters, $i$ is the current, $v$ is the scan rate. The current density is controlled by the non-diffusion processes (capacitive effect) when b = 1, otherwise, current density is due to diffusion-controlled redox intercalation process (battery- type behavior) and b = 0.5. The calculated b-values of $CuMnO_2$-rGO during cathodic scan are shown in Fig. S9. At the peak

11

potential between 0.1 to 0.2 V, the b-value are in the range 0.92 to 1.0, confirming that the current

is predominantly capacitive. At the peak between 0.3 to 0.4 V, the b-value are in the range of 0.65

to 0.7; suggesting coexistence of both diffusion-controlled and capacitive processes.

It should be noted that $CuMnO_2$-rGO/NF exhibits diffusion-controlled (battery-type behavior) in

addition to capacitive behavior. The current response at a fixed potential $i(v)$ can be described as

the combination of capacitive effects ($k_1 v$) and diffusion-controlled reactions ($k_2 v^{1/2}$) according

to[47]:

$$i(v) = k_1 v + k_2 v^{1/2} \qquad (9)$$

$k_1$ and $k_2$ can be calculated from from the slope and the $y$-axis intercept point of The plots of $v^{1/2}$

versus $i(v)/ v^{1/2}$ (Fig. 3d). Fig. 3e shows the contribution fraction of capacitive effect at different

scan rate. It can be concluded that the charge storage behavior predominantly originated from redox

reaction (diffusion-controlled process). Furthermore, the capacitive contribution increased with the

increase of scan rate due to insufficient time for ion diffusion into deeper site and redox process.

Furthermore, the electrochemical stability of the $CuMnO_2$/NF and $CuMnO_2$-rGO/NF electrodes

were investigated up to 5000 cycles at a scan rate of 100 mV s$^{-1}$. The variation of the specific

capacitance of both electrodes gradually increased during the initial 3000 cycle, then it became

steady up to 5000 cycles (Fig. 3f), due to the the gradual activation of the electrode surface and

proliferation of available active sites and thus complete accessibility to the deeper active cite after

3000 cycles [18, 19, 48, 49]. The increased value for the $CuMnO_2$/NF and $CuMnO_2$-rGO/NF

electrodes was calculated as around 17% and 25%, respectively. The superior cyclic stability of

$CuMnO_2$-rGO/NF over the $CuMnO_2$/NF may be originated from the interaction of rGO and

$CuMnO_2$. The rGO nanosheets offer high surface area that leads to enhanced mechanical and

structural stability of the nanocomposite. Fig. S10 shows the CV curves of the $CuMnO_2$-rGO/NF

electrode during 5000 cycles.

12

The excellent capacitive performance of the $CuMnO_2$-rGO/NF electrode was also verified from galvanostatic charge/discharge (GCD) studies over the voltage window of -0.2-0.5 V (Fig. 4a). A longer discharge time corresponds to a larger capacitance of the CuMnO2-rGO/NF electrode, due to a synergetic effect between rGO and $CuMnO_2$ and an enhanced effective surface area required for ion exchange. The nonlinear discharge curves with negligible potential drop further resemble the pseudocapacitive behaviour and excellent capacitive performance of the electrode materials, which was in accordance with the CV results. Inset of Fig. 4a represents the current density dependence on the specific capacitance values. With changing the current densities from 3 to 10 A $g^{-1}$, the $CuMnO_2$-rGO/NF electrode showed higher rate stability (81%) than the CuMnO2/NF electrode (76%). The superior rate capability of the $CuMnO_2$-rGO/NF electrode is attributed to the shorter diffusion length of ions, the larger surface area, and the increased electrical conductivity of the $CuMnO_2$-rGO nanostructure. GCD curves of the $CuMnO_2$/NF and $CuMnO_2$-rGO/NF electrodes at different current densities are also shown in Fig. S11. Moreover, the specific capacitance of both electrodes calculated by mAh $g^{-1}$ at various current density and scan rate, are shown in Fig. S12. The EIS analysis was conducted to estimate kinetic parameters of the $CuMnO_2$/NF and $CuMnO_2$-rGO/NF electrodes in a frequency range from 0.1 Hz to 100 kHz at open circuit potentials (Fig. 4b). The Nyquist plots of the two electrodes are composed of the distorted semicircles in the high-medium frequency region and straight lines in the low frequency region, which describes interfacial charge-transfer resistance ($R_{ct}$) and diffusion resistance in the electroactive material, respectively [50, 51]. The $R_{ct}$ value is 3.3 and 4.5 Ω for the $CuMnO_2$-rGO/NF and $CuMnO_2$/NF electrodes, respectively. The $CuMnO_2$-rGO/NF electrode displays a more vertical line (75°) than the $CuMnO_2$/NF electrode (60°); demonstrating the lower diffusion resistance and more ideal capacitive behavior. The effective cooperation of graphene nanosheets as conductive framework in the $CuMnO_2$-rGO nanocomposite is the imminent cause of

13

electrochemical performance improvement. As shown in inset of Fig. 4b, the Nyquist plots of the CuMnO$_2$-rGO/NF electrode display similar features before and after 5000 charge/discharge cycles with negligible changes in the electrochemical parameters based on the electrical equivalent circuit analysis (Scheme S1 and Table S1). This is a clear evidence of the excellent electrochemical and physical stability of the CuMnO$_2$-rGO/NF electrode. Also, the small increase in the R$_{ct}$ (from 3.35 to 6.7) indicates the small changes and deformation of the morphology and structure of CuMnO$_2$-rGO during successive potential cycles. Additionally, the diffusion line angle after 5000 cycles shows small decrease compared to the initial diffusion line slope; suggesting the insignificant changes in the electrolyte penetration and ion diffusion resistance of the electrode material.

*3.3 Electrochemical performance of the asymmetric supercapacitor (ASC)*

Designing ASCs is an efficient pathway to boost energy density of supercapacitors. Assembling a positive electrode (CuMnO$_2$-rGO/NF) with a pseudocapacitive behavior and an EDLC negative electrode (rGO/NF) into an ASC (denoted rGO/NF//CuMnO$_2$-rGO/NF) with an aqueous electrolyte can greatly enhance energy density because of the increased specific capacitance by Faradic redox reaction on side of positive electrode and the broadened potential window via the high overpotential of the reversible hydrogen electro-sorption on the side of the carbon EDLC electrodes according to the relationship of $E = 1/2CV^2$ [15]. The weight ratio of the negative electrode to the positive electrode is calculated to be 6.85 based on the charge balancing theory, and the maximum voltage range of the device was controlled by the voltage range of each electrode in a three-electrode system. As seen in Fig. 5a, the voltage range of the rGO/NF electrode is between -1.0 and 0.0 V with a quasi-rectangular behavior, while the range of the CuMnO2-rGO/NF electrode is between -0.2 to 0.7 V with a pseudocapacitive behavior. Thus, the CV curves of rGO/NF//CuMnO$_2$-rGO/NF ASC can be monitored between 0.0 to 1.9 V (Fig. 5b). It can be seen

14

that the evolution of oxygen occurred at a voltage exceeding 1.7 V [52]. Consequently, 1.7 V was chosen as the suitable voltage for our electrochemical studies. Fig. 5c illustrates the CV curves of the ASC at different scan rates in the range from 0.0 to 1.7 V. As expected, defined redox peaks were observed, which implies the rationale of the combination of pseudocapacitive and EDLC electrodes. Notably, the shape of the CV curves was well maintained with increasing scan rate, indicating good rate capability and favourable capacitive property of the ASC. The long-term stability was evaluated at a scan rate of 100 mV s$^{-1}$ (Fig. 5d). The specific capacitance increased up to 1500 cycles, and a deterioration of only 3.3% was observed in the subsequent 2500 cycles. Nyquist plots of the ASC reveal a small change of Rct after 4000 cycles and proves little performance degradation (Fig. S13).

GCD was investigated at different current densities within the same voltage window as the CV measurement, and the corresponding profiles are presented in Fig. 5e. The nearly symmetric shapes and a small internal resistance (IR) drop corroborate ideal characteristics of the ASC device. Considering the total mass of the active material in both electrodes (almost 2 mg) and the discharge time, the specific capacitances were estimated to be 93, 88, 86, 82, 80, 74, and 73 F g$^{-1}$ at current densities of 2, 2.5, 3, 3.5, 4, 4.5 and 5 A g$^{-1}$, respectively. Since power density and energy density are two dominant parameters to assess the potential application of the ASC, these parameters were calculated and results are depicted as the Ragone plot (Fig. 5f). Our device delivered a maximum energy density of 37.5 Wh kg$^{-1}$ at a power density of 1700 W kg$^{-1}$ and a high energy density of 29.5 Wh kg$^{-1}$ at a high power density of 4250 W kg$^{-1}$. The obtained maximum energy density is among the highest results of manganese and copper-based ASCs [53-63]. A detailed comparison between the proposed nanocomposites and the previously reported composites is listed in Table S2, where performance is compared in both three- and two-electrode systems.

15

## 4. Conclusions

In summary, a simple hydrothermal method was used for the in-situ synthesis of $CuMnO_2$ and $CuMnO_2$-rGO nanocomposite on nickel foam substrate. The $CuMnO_2$-rGO/NF electrode exhibited better electrochemical performance than the $CuMnO_2$/NF electrode. The $CuMnO_2$-rGO/NF electrode displayed a high specific capacitance (1727 F $g^{-1}$ at 3 A $g^{-1}$), good rate capability (19% loss at 10 A $g^{-1}$) and great cycling stability (retention of 125% up to 5000 cycles). Furthermore, an asymmetric supercapacitor was constructed by coupling with the rGO negative electrode (rGO/NF//$CuMnO_2$-rGO/NF). The supercapacitor demonstrated a considerable specific capacitance (93 F $g^{-1}$ at 2 A $g^{-1}$), excellent cycling stability (decay of 3.3% up to 4000 cycles), high energy density (37.5 Wh $kg^{-1}$) and high power density (4250 W $kg^{-1}$). Our results offer a compelling evidence of the $CuMnO_2$-rGO composite as a promising material for actual application.

**Notes**

The authors declare no conflict of interest.

**References:**

[1] Y. Han, N. Hu, S. Liu, Z. Hou, J. Liu, X. Hua, Z. Yang, L. Wei, L. Wang, H. Wei, Nanocoating covalent organic frameworks on nickel nanowires for greatly enhanced-performance supercapacitors, Nanotechnology 28 (2017) 33LT01.

[2] S. Kazemi, A. Asghari, High performance supercapacitors based on the electrodeposited $Co_3O_4$ nanoflakes on electro-etched carbon fibers, Electrochim. Acta 138 (2014) 9-14.

[3] S.H. Kazemi, B. Karimi, S.A. Aghdam, H. Behzadnia, M.A. Kiani, Polyaniline–ionic liquid derived ordered mesoporous carbon nanocomposite: synthesis and supercapacitive behavior, RSC Adv. 5 (2015) 69032-69041.

[4] S. Liu, L. Yao, Y. Lu, X. Hua, J. Liu, Z. Yang, H. Wei, Y. Mai, All-organic covalent organic framework/polyaniline composites as stable electrode for high-performance supercapacitors, Mater. Lett. 236 (2019) 354-357.

[5] H. Zhao, C. Wang, R. Vellacheri, M. Zhou, Y. Xu, Q. Fu, M. Wu, F. Grote, Y. Lei, Self-Supported Metallic Nanopore Arrays with Highly Oriented Nanoporous Structures as Ideally Nanostructured Electrodes for Supercapacitor Applications, Adv. Mater. 26 (2014) 7654-7659.

[6] F. Bahmani, S.H. Kazemi, H. Kazemi, M. Kiani, S.Y. Feizabadi, Nanocomposite of copper–molybdenum–oxide nanosheets with graphene as high-performance materials for supercapacitors, J. Alloys Compd. 784 (2019) 500-512.

[7] L. Wen, Y. Mi, C. Wang, Y. Fang, F. Grote, H. Zhao, M. Zhou, Y. Lei, Cost-effective Atomic Layer Deposition Synthesis of Pt Nanotube Arrays: Application for High Performance Supercapacitor, Small 10 (2014) 3162-3168.

[8] M. Zhou, Y. Xu, C. Wang, Q. Li, J. Xiang, L. Liang, M. Wu, H. Zhao, Y. Lei, Amorphous $TiO_2$ inverse opal anode for high-rate sodium ion batteries, Nano Energy 31 (2017) 514-524.

[9] S.H. Kazemi, F. Bahmani, H. Kazemi, M. Kiani, Binder-free electrodes of $NiMoO_4$/graphene oxide nanosheets: synthesis, characterization and supercapacitive behavior, RSC Adv. 6 (2016) 111170-111181.

[10] Q. Liao, N. Li, S. Jin, G. Yang, C. Wang, All-solid-state symmetric supercapacitor based on $Co_3O_4$ nanoparticles on vertically aligned graphene, Acs Nano 9 (2015) 5310-5317.

[11] H. Zhu, C. Xiao, H. Cheng, F. Grote, X. Zhang, T. Yao, Z. Li, C. Wang, S. Wei, Y. Lei, Magnetocaloric effects in a freestanding and flexible graphene-based superlattice synthesized with a spatially confined reaction, Nature Commun.5 (2014) 3960.

[12] M. Han, A. Jayakumar, Z. Li, Q. Zhao, J. Zhang, X. Jiang, X. Guo, R. Wang, C. Xu, S. Song, J.-M. Lee, N. Hu, Fabricating 3D Macroscopic Graphene-Based Architectures with Outstanding Flexibility by the Novel Liquid Drop/Colloid Flocculation Approach for Energy Storage Applications, ACS Appl. Mater. Interfaces 10 (2018) 21991-22001.

[13] L. Peng, X. Peng, B. Liu, C. Wu, Y. Xie, G. Yu, Ultrathin two-dimensional $MnO_2$/graphene hybrid nanostructures for high-performance, flexible planar supercapacitors, Nano lette. 13 (2013) 2151-2157.

[14] D. Moitra, C. Anand, B.K. Ghosh, M. Chandel, N.N. Ghosh, One-Dimensional $BiFeO_3$ Nanowire-Reduced Graphene Oxide Nanocomposite as Excellent Supercapacitor Electrode Material, ACS Appl. Energy Mater. 1 (2018) 464-474.

[15] S.K. Kaverlavani, S. Moosavifard, A. Bakouei, Designing graphene-wrapped nanoporous $CuCo_2O_4$ hollow spheres electrodes for high-performance asymmetric supercapacitors, J. Mater. Chem. A 5 (2017) 14301-14309.

[16] H. Ma, J. He, D.-B. Xiong, J. Wu, Q. Li, V. Dravid, Y. Zhao, Nickel cobalt hydroxide@ reduced graphene oxide hybrid nanolayers for high performance asymmetric supercapacitors with remarkable cycling stability, ACS Appl. Mater. Interfaces 8 (2016) 1992-2000.

[17] L. Liang, Y. Xu, Y. Lei, H. Liu, 1-Dimensional $AgVO_3$ nanowires hybrid with 2-dimensional graphene nanosheets to create 3-dimensional composite aerogels and their improved electrochemical properties, Nanoscale 6 (2014) 3536-3539.

[18] H. Niu, X. Yang, H. Jiang, D. Zhou, X. Li, T. Zhang, J. Liu, Q. Wang, F. Qu, Hierarchical core–shell heterostructure of porous carbon nanofiber@ $ZnCo_2O_4$ nanoneedle arrays: advanced binder-free electrodes for all-solid-state supercapacitors, J. Mater. Chem. A 3 (2015) 24082-24094.

[19] Y. Zhang, L. Li, H. Su, W. Huang, X. Dong, Binary metal oxide: advanced energy storage materials in supercapacitors, J. Mater. Chem. A 3 (2015) 43-59.

[20] M. Abdollahifar, S.-S. Huang, Y.-H. Lin, Y.-C. Lin, B.-Y. Shih, H.-S. Sheu, Y.-F. Liao, N.-L. Wu, High-performance carbon-coated $ZnMn_2O_4$ nanocrystallite supercapacitors with tailored microstructures enabled by a novel solution combustion method, J. Power Sources 378 (2018) 90-97.

[21] Z. Wang, Z. Zhu, C. Zhang, C. Xu, C. Chen, Facile synthesis of reduced graphene oxide/$NiMn_2O_4$ nanorods hybrid materials for high-performance supercapacitors, Electrochim. Acta 230 (2017) 438-444.

[22] Y. Xu, X. Wang, C. An, Y. Wang, L. Jiao, H. Yuan, Facile synthesis route of porous $MnCo_2O_4$ and $CoMn_2O_4$ nanowires and their excellent electrochemical properties in supercapacitors, J. Mater. Chem. A 2 (2014) 16480-16488.

[23] F. Grote, R.-S. Kühnel, A. Balducci, Y. Lei, Template assisted fabrication of free-standing $MnO_2$ nanotube and nanowire arrays and their application in supercapacitors, Appl. Phys. Lett. 104 (2014) 053904.

[24] M. Huang, F. Li, F. Dong, Y.X. Zhang, L.L. Zhang, $MnO_2$-based nanostructures for high-performance supercapacitors, J. Mater. Chem. A 3 (2015) 21380-21423.

[25] G. Yu, L. Hu, N. Liu, H. Wang, M. Vosgueritchian, Y. Yang, Y. Cui, Z. Bao, Enhancing the supercapacitor performance of graphene/$MnO_2$ nanostructured electrodes by conductive wrapping, Nano lett. 11 (2011) 4438-4442.

[26] L. Wang, M. Arif, G. Duan, S. Chen, X. Liu, A high performance quasi-solid-state supercapacitor based on $CuMnO_2$ nanoparticles, J. Power Sources 355 (2017) 53-61.

[27] F. Luan, G. Wang, Y. Ling, X. Lu, H. Wang, Y. Tong, X.-X. Liu, Y. Li, High energy density asymmetric supercapacitors with a nickel oxide nanoflake cathode and a 3D reduced graphene oxide anode, Nanoscale 5 (2013) 7984-7990.

[28] Y. Wei, H. Liu, Y. Jin, K. Cai, H. Li, Y. Liu, Z. Kang, Q. Zhang, Carbon nanoparticle ionic liquid functionalized activated carbon hybrid electrode for efficiency enhancement in supercapacitors, New J. Chem. 37 (2013) 886-889.

[29] A. Sumboja, C.Y. Foo, X. Wang, P.S. Lee, Large areal mass, flexible and free-standing reduced graphene oxide/manganese dioxide paper for asymmetric supercapacitor device, Adv. Mater. 25 (2013) 2809-2815.

[30] X. Mu, J. Du, Y. Zhang, Z. Liang, H. Wang, B. Huang, J. Zhou, X. Pan, Z. Zhang, E. Xie, Construction of Hierarchical CNT/rGO-Supported MnMoO4 Nanosheets on Ni Foam for High-Performance Aqueous Hybrid Supercapacitors, ACS Appl. Mater. Interfaces 9 (2017) 35775-35784.

[31] D. Du, R. Lan, W. Xu, R. Beanland, H. Wang, S. Tao, Preparation of a hybrid $Cu_2O$/$CuMoO_4$ nanosheet electrode for high-performance asymmetric supercapacitors, J. Mater. Chem. A 4 (2016) 17749-17756.

[32] D. Xiong, Q. Zhang, Z. Du, S.K. Verma, H. Li, X. Zhao, Low temperature hydrothermal synthesis mechanism and thermal stability of p-type $CuMnO_2$ nanocrystals, New J. Chem. 40 (2016) 6498-6504.

[33] S. Zhu, J. Guo, J. Dong, Z. Cui, T. Lu, C. Zhu, D. Zhang, J. Ma, Sonochemical fabrication of $Fe_3O_4$ nanoparticles on reduced graphene oxide for biosensors, Ultrason. Sonochem. 20 (2013) 872-880.

20

[34] J. Tang, J. Shen, N. Li, M. Ye, One-pot tertbutanol assisted solvothermal synthesis of $CoNi_2S_4$/reduced graphene oxide nanocomposite for high-performance supercapacitors, Ceram. Int. 41 (2015) 6203-6211.

[35] X. Zhang, L. Yao, S. Liu, Q. Zhang, Y. Mai, N. Hu, H. Wei, High-performance lithium sulfur batteries based on nitrogen-doped graphitic carbon derived from covalent organic frameworks, Mater. Today Energy 7 (2018) 141-148.

[36] S. Claramunt, A. Varea, D. López-Díaz, M.M. Velázquez, A. Cornet, A. Cirera, The importance of interbands on the interpretation of the Raman spectrum of graphene oxide, J. Phys. Chem. C 119 (2015) 10123-10129.

[37] D. Ghosh, J. Lim, R. Narayan, S.O. Kim, High energy density all solid state asymmetric pseudocapacitors based on free standing reduced graphene oxide-$Co_3O_4$ composite aerogel electrodes, ACS Appl. Mater. Interfaces 8 (2016) 22253-22260.

[38] S. Karthick, H.-S. Lee, S.-J. Kwon, R. Natarajan, V. Saraswathy, Standardization, calibration, and evaluation of tantalum-nano rGO-$SnO_2$ composite as a possible candidate material in humidity sensors, Sensors 16 (2016) 2079.

[39] K. Krishnamoorthy, M. Veerapandian, R. Mohan, S.-J. Kim, Investigation of Raman and photoluminescence studies of reduced graphene oxide sheets, Appl. Phys. A 106 (2012) 501-506.

[40] H. Park, J. Kwon, H. Choi, D. Shin, T. Song, X.W.D. Lou, Unusual $Na^+$ Ion Intercalation/Deintercalation in Metal-Rich Cu1. 8S for Na-Ion Batteries, ACS nano 12 (2018) 2827-2837.

[41] M. Ye, X. Wen, N. Zhang, W. Guo, X. Liu, C. Lin, In situ growth of CuS and $Cu_{1.8}S$ nanosheet arrays as efficient counter electrodes for quantum dot-sensitized solar cells, J. Mater. Chem. A 3 (2015) 9595-9600.

[42] K. Lei, X. Han, Y. Hu, X. Liu, L. Cong, F. Cheng, J. Chen, Chemical etching of manganese oxides for electrocatalytic oxygen reduction reaction, Chem. Commun. 51 (2015) 11599-11602.

[43] Z. Wang, Y. Dong, H. Li, Z. Zhao, H.B. Wu, C. Hao, S. Liu, J. Qiu, X.W.D. Lou, Enhancing lithium–sulphur battery performance by strongly binding the discharge products on amino-functionalized reduced graphene oxide, Nature Commun.5 (2014) 5002.

[44] L. Shen, L. Du, S. Tan, Z. Zang, C. Zhao, W. Mai, Flexible electrochromic supercapacitor hybrid electrodes based on tungsten oxide films and silver nanowires, Chem. Commun. 52 (2016) 6296-6299.

[45] S. Sarkar, P. Howli, B. Das, N.S. Das, M. Samanta, G.C. Das, K.K. Chattopadhyay, Novel Quaternary Chalcogenide/Reduced Graphene Oxide-Based Asymmetric Supercapacitor with High Energy Density, ACS Appl. Mater. Interfaces 9 (2017) 22652-22664.

[46] R. Wang, C. Xu, J.-M. Lee, High performance asymmetric supercapacitors: New NiOOH nanosheet/graphene hydrogels and pure graphene hydrogels, Nano Energy 19 (2016) 210-221.

[47] M. Liang, M. Zhao, H. Wang, J. Shen, X. Song, Enhanced cycling stability of hierarchical $NiCo_2S_4$@ $Ni(OH)_2$@ PPy core–shell nanotube arrays for aqueous asymmetric supercapacitors, J. Mater. Chem. A  6 (2018) 2482-2493.

[48] S.H. Kazemi, B. Hosseinzadeh, H. Kazemi, M.A. Kiani, S. Hajati, Facile Synthesis of Mixed Metal–Organic Frameworks: Electrode Materials for Supercapacitors with Excellent Areal Capacitance and Operational Stability, ACS Appl. Mater. Interfaces 10 (2018) 23063-23073.

[49] X. Liu, S. Shi, Q. Xiong, L. Li, Y. Zhang, H. Tang, C. Gu, X. Wang, J. Tu, Hierarchical $NiCo_2O_4$@$NiCo_2O_4$ Core/Shell Nanoflake Arrays as High-Performance Supercapacitor Materials, ACS Appl. Mater. Interfaces 5 (2013) 8790-8795.

[50] H.S. Chavan, B. Hou, A.T.A. Ahmed, Y. Jo, S. Cho, J. Kim, S.M. Pawar, S. Cha, A.I. Inamdar, H. Im, Nanoflake $NiMoO_4$ based smart supercapacitor for intelligent power balance monitoring, Sol. Energy Mater. Sol. Cells 185 (2018) 166-173.

[51] X. Guo, T. Zheng, G. Ji, N. Hu, C. Xu, Y. Zhang, Core/shell design of efficient electrocatalysts based on $NiCo_2O_4$ nanowires and NiMn LDH nanosheets for rechargeable zinc–air batteries, J. Mater. Chem. A 6 (2018) 10243-10252.

[52] D. Cheng, Y. Yang, J. Xie, C. Fang, G. Zhang, J. Xiong, Hierarchical $NiCo_2O_4$@ $NiMoO_4$ core–shell hybrid nanowire/nanosheet arrays for high-performance pseudocapacitors, J. Mater. Chem. A 3 (2015) 14348-14357.

[53] C. Dong, Y. Wang, J. Xu, G. Cheng, W. Yang, T. Kou, Z. Zhang, Y. Ding, 3D binder-free $Cu_2O$@ Cu nanoneedle arrays for high-performance asymmetric supercapacitors, J. Mater. Chem. A 2 (2014) 18229-18235.

[54] D.P. Dubal, N.R. Chodankar, G.S. Gund, R. Holze, C.D. Lokhande, P. Gomez-Romero, Asymmetric supercapacitors based on hybrid CuO@ reduced graphene oxide@ sponge versus reduced graphene oxide@ sponge electrodes, Energy Technol. 3 (2015) 168-176.

[55] H. Gao, F. Xiao, C.B. Ching, H. Duan, High-performance asymmetric supercapacitor based on graphene hydrogel and nanostructured $MnO_2$, ACS Appl. Mater. Interfaces 4 (2012) 2801-2810.

[56] M. Jing, H. Hou, Y. Yang, Y. Zhu, Z. Wu, X. Ji, Electrochemically alternating voltage tuned $Co_2MnO_4$/Co hydroxide chloride for an asymmetric supercapacitor, Electrochim. Acta 165 (2015) 198-205.

[57] X. Meng, L. Lu, C. Sun, Green Synthesis of Three-Dimensional $MnO_2$/Graphene Hydrogel Composites as a High-Performance Electrode Material for Supercapacitors, ACS Appl. Mater. Interfaces 10 (2018) 16474-16481.

[58] S.E. Moosavifard, M.F. El-Kady, M.S. Rahmanifar, R.B. Kaner, M.F. Mousavi, Designing 3D highly ordered nanoporous CuO electrodes for high-performance asymmetric supercapacitors, ACS Appl. Mater. Interfaces 7 (2015) 4851-4860.

[59] A. Shanmugavani, R.K. Selvan, Improved electrochemical performances of $CuCo_2O_4$/CuO nanocomposites for asymmetric supercapacitors, Electrochim. Acta 188 (2016) 852-862.

[60] Y. Wang, C. Shen, L. Niu, R. Li, H. Guo, Y. Shi, C. Li, X. Liu, Y. Gong, Hydrothermal synthesis of $CuCo_2O_4$/CuO nanowire arrays and $RGO/Fe_2O_3$ composites for high-performance aqueous asymmetric supercapacitors, J. Mater. Chem. A 4 (2016) 9977-9985.

[61] J. Yang, G. Li, Z. Pan, M. Liu, Y. Hou, Y. Xu, H. Deng, L. Sheng, X. Zhao, Y. Qiu, All-Solid-State High-Energy Asymmetric Supercapacitors Enabled by Three-Dimensional Mixed-Valent MnO x Nanospike and Graphene Electrodes, ACS Appl. Mater. Interfaces 7 (2015) 22172-22180.

[62] N. Yu, H. Yin, W. Zhang, Y. Liu, Z. Tang, M.Q. Zhu, High-Performance Fiber-Shaped All-Solid-State Asymmetric Supercapacitors Based on Ultrathin $MnO_2$ Nanosheet/Carbon Fiber Cathodes for Wearable Electronics, Adv. Energy Mater. 6 (2016).

[63] S.J. Zhu, J.Q. Jia, T. Wang, D. Zhao, J. Yang, F. Dong, Z.G. Shang, Y.X. Zhang, Rational design of octahedron and nanowire $CeO_2$@ $MnO_2$ core–shell heterostructures with outstanding rate capability for asymmetric supercapacitors, Chem. Commun. 51 (2015) 14840-14843.
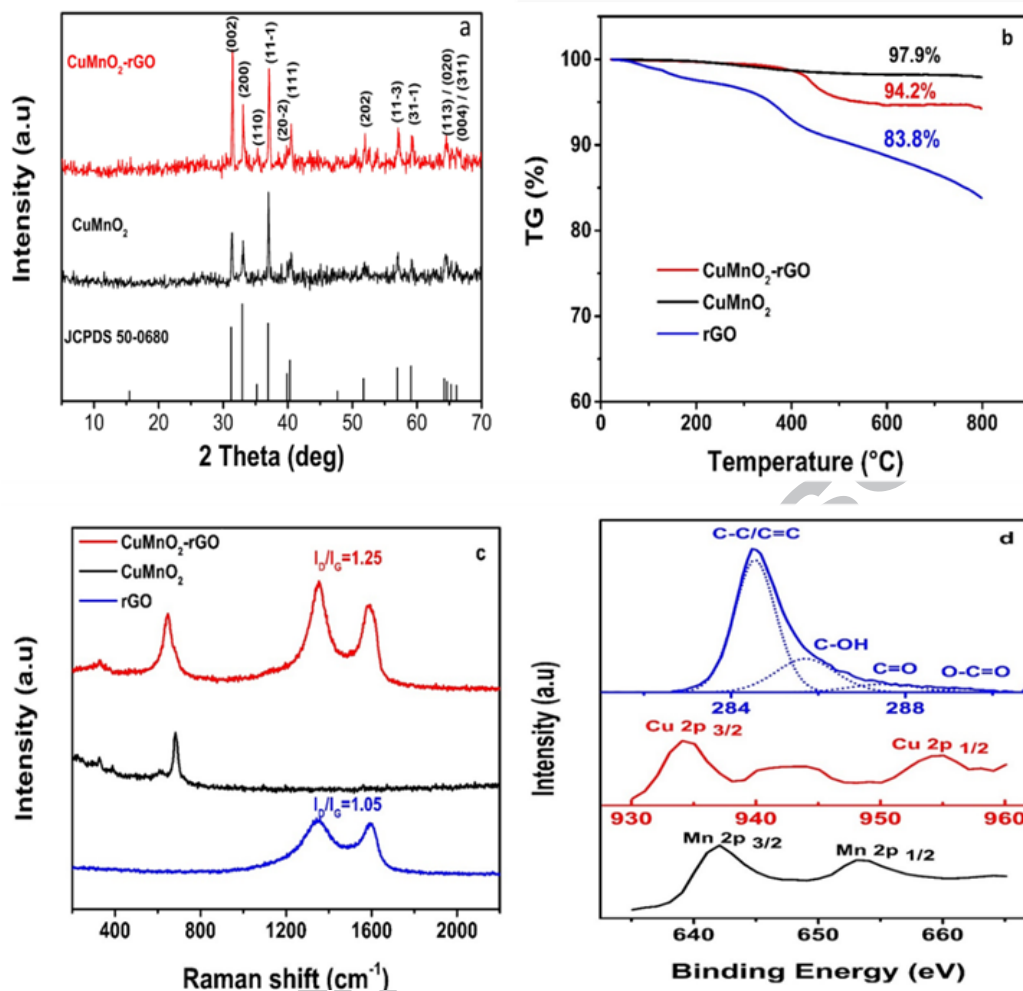
**Figure 1.** Structural and composition characterization of CuMnO$_2$ and CuMnO$_2$-rGO nanocomposite: (a) XRD patterns, (b) TGA curves, (c) Raman spectra, and (d) core level XPS spectra of Cu 2p, Mn 2p and of CuMnO$_2$-rGo nanocomposite.
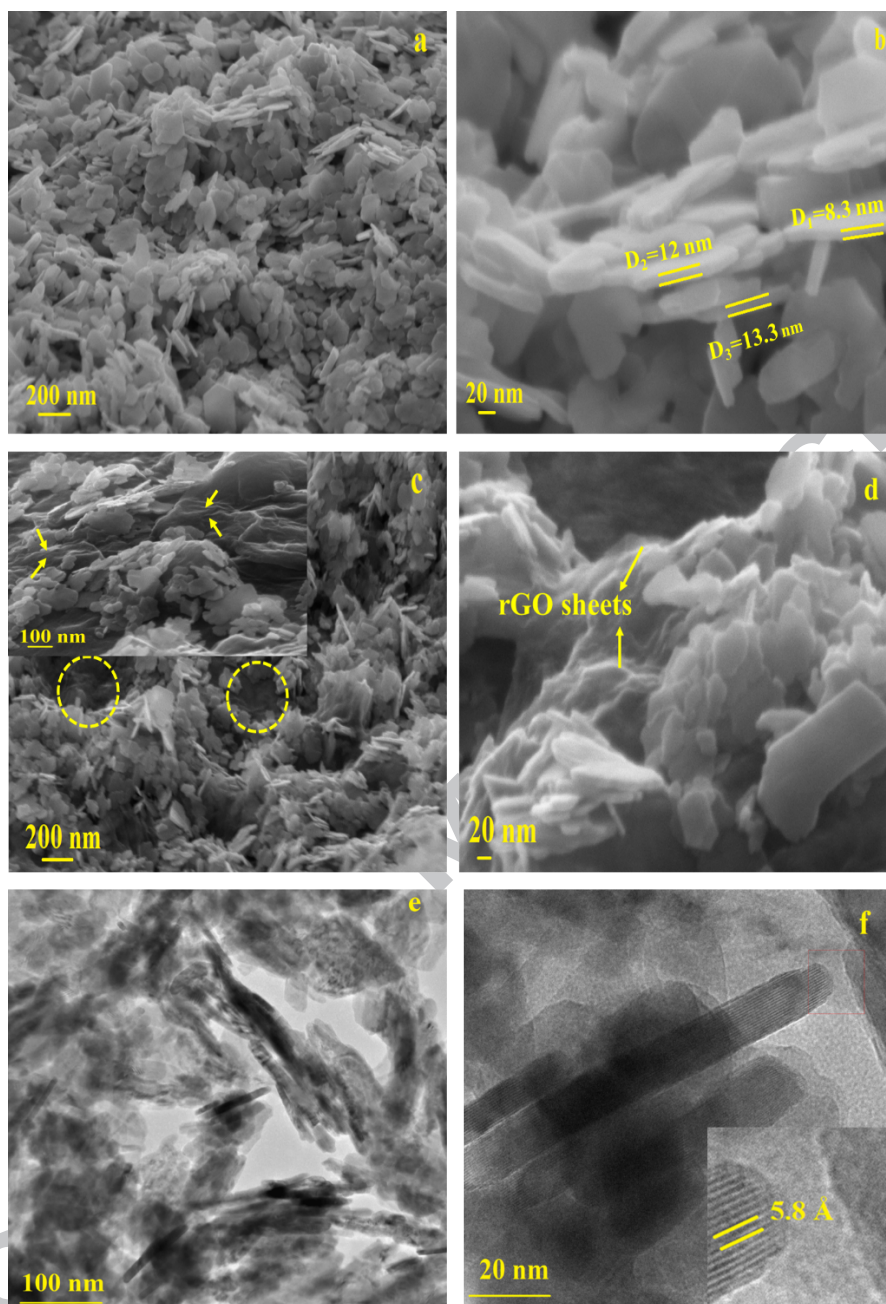
**Figure 2.** SEM images of (a, b) $CuMnO_2$/NF and (c, d) $CuMnO_2$-rGO/NF. (e, f) TEM images of $CuMnO_2$-rGO nanocomposite (inset in f: HRTEM image).
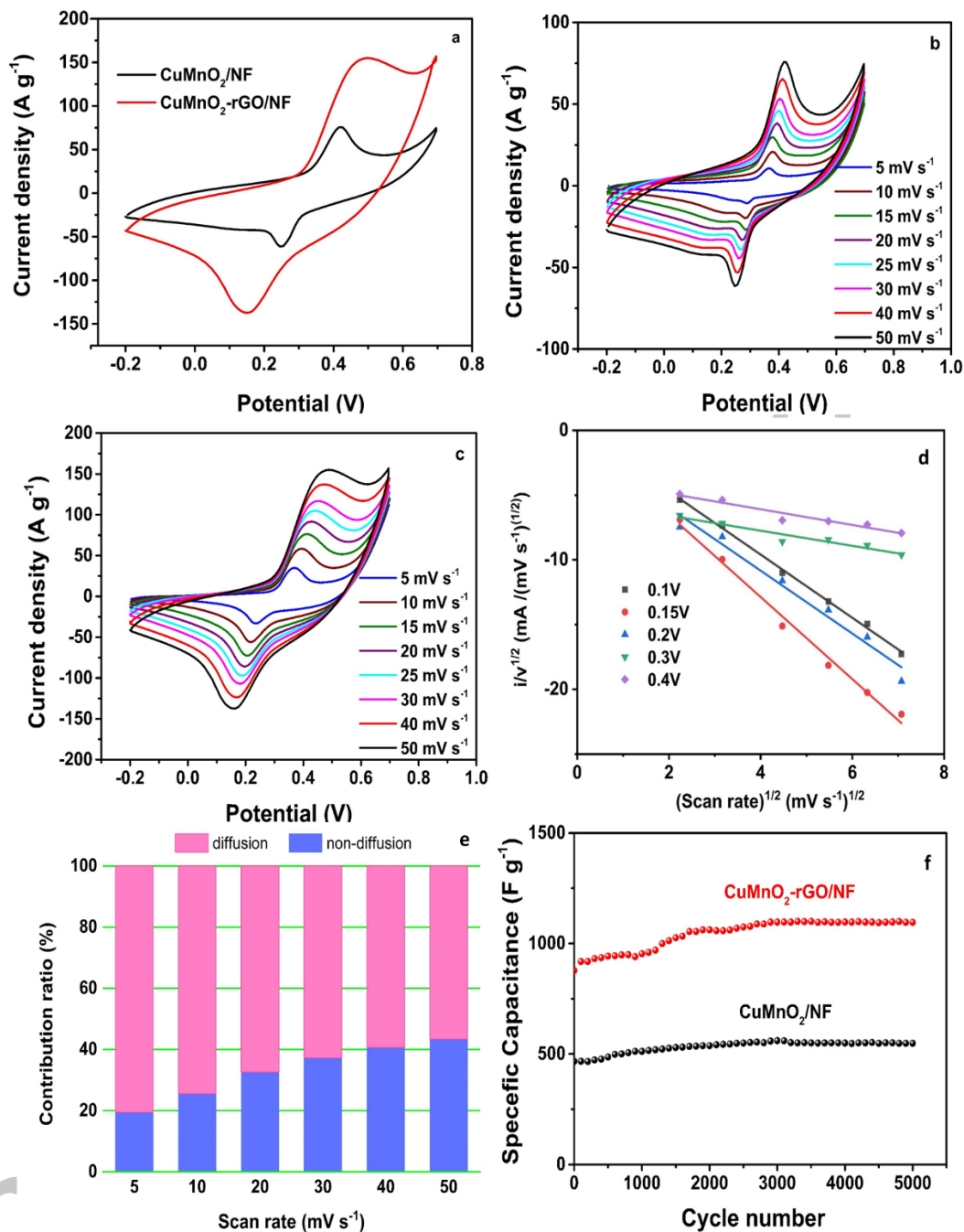
**Figure 3.** CV curves of (a) CuMnO$_2$/NF and CuMnO$_2$-rGO/NF electrodes at a scan rate of 50 mV s$^{-1}$, (b) CuMnO$_2$/NF, (c) CuMnO$_2$-rGO/NF electrodes at different scan rates, (d) The plots of $i$(v)/ $v^{1/2}$ versus $v^{1/2}$ at different potentials of the cathodic scan, (e) Capacitive and diffusion controlled contribution to the charge storage at different scan rate and (f) cycling stability of CuMnO$_2$/NF and CuMnO$_2$-rGO/NF electrodes at scan rate 100 mV s$^{-1}$.
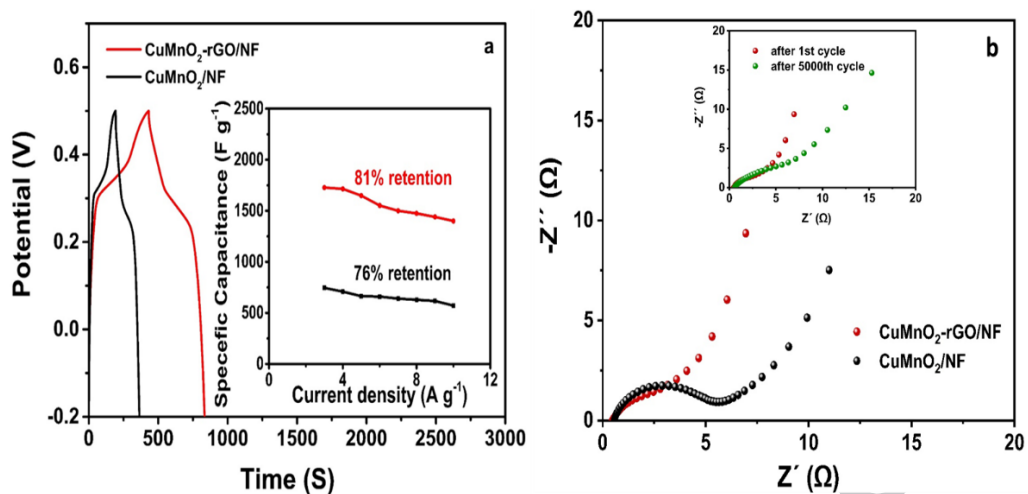
27

**Figure 4.** (a) GCD of CuMnO$_2$/NF and CuMnO$_2$-rGO/NF electrodes at 3 A g$^{-1}$ (inset: variation of specific capacitance as a function of current density). (b) Nyquist plots of CuMnO$_2$/NF and CuMnO$_2$-rGO/NF electrodes (inset: Nyquist plots of CuMnO$_2$-rGO/NF electrode after the 1st and 5000th cycle).
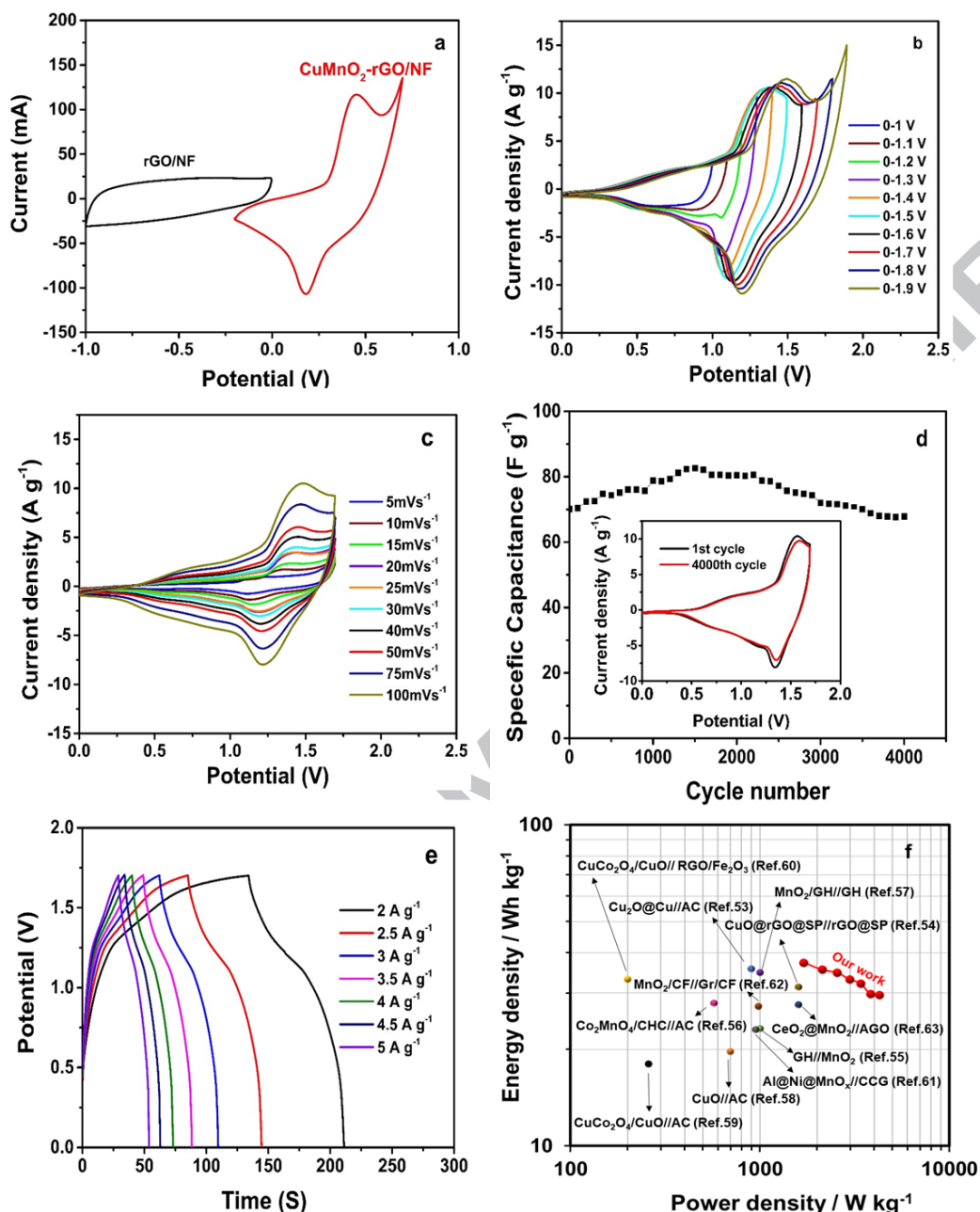
**Figure 5.** CV curves of (a) rGO/NF and CuMnO$_2$-rGO/NF electrode in a three-electrode system at scan rate 30 mV s$^{-1}$, asymmetric rGO/NF//CuMnO$_2$-rGO/NF supercapacitor within different potential ranges (b) and at different scan rates in potential ranges of 0 to 1.7 V (c). (d) Cycling stability as a function of cycle number (inset: CV curves before and after 4000 cycles). (e) GCD curves at different current densities. (f) Ragone plot of the asymmetric rGO/NF//CuMnO$_2$-rGO /NF supercapacitor.

**Highlights**

- Direct deposition of rGO-CuMnO$_2$ on Ni foam was done through hydrothermal method.

- The rGO-CuMnO$_2$/NF is a free-standing CuMnO$_2$ electrode for supercapacitors.

- A specific capacitance of 1727 F g$^{-1}$ was achieved for the rGO-CuMnO$_2$/NF electrode.

- The rGO-CuMnO$_2$/NF electrode showed an excellent cycle life stability.

- The rGO-CuMnO$_2$ based asymmetric device delivered an energy density of 37.5 Wh kg$^{-1}$.